# Theoretical Clues to the Mechanism of Dioxygen Formation at the Oxygen-Evolving Complex of Photosystem II

**Gabriel Aullón, Eliseo Ruiz, and Santiago Alvarez*[a]**

**Abstract:** The mechanism of the generation of dioxygen at the oxygen-evolving complex (OEC) of photosystem II (PSII), a crucial step in photosynthesis, is still under debate. The simplest unit present in the OEC that can produce $O_2$ is a dinuclear oxo-bridged manganese complex within the tetranuclear $Mn_4$ cluster. In this paper we report a theoretical study of the model complexes $[Mn_2(\mu\text{-}O)_2(NH_3)_6(H_2O)_2]^{n+}$ $(n=2-5)$, for which density functional calculations have been carried out for several electronic configurations. The molecular orbital picture deduced from the calculations indicates that one-electron oxidation of the $Mn_2^{IV,IV}/(O^{2-})_2$ complex $(n=4)$ mostly affects the oxygen atoms, thus ruling out the existence of a $Mn^V$ oxidation state in this context, while the incipient formation of an O–O bond in the $O_2^{3-}$ transient species evolves exothermally toward the dissociation of dioxygen and a $Mn_2^{II,III}$ couple. These results identify the electronic features that could be needed to enable an intramolecular mechanism of oxygen–oxygen bond formation to exist at the OEC during photosynthesis.

**Keywords:** bioinorganic chemistry · dioxygen · electronic structure · manganese · photosynthesis

## Introduction

The photosystem II reaction center (PSII), one of the most interesting manganese-containing enzymes,[1] is a fascinating molecular machine that is employed by green plants and algae to absorb light and generate oxygen from water [Eq. (1)].

$$2H_2O + h\nu \rightarrow O_2 + 4e^- + 4H^+ \quad (1)$$

There is a wealth of experimental evidence indicating that this process occurs with the help of a tetranuclear manganese cluster, in which oxo bridges probably link the Mn atoms. It is usually referred to as the *oxygen-evolving complex* (OEC) or *water-oxidizing complex* (WOC). Several structural models have been proposed for such a cluster, including the two shown in **1**.[2, 3] The cubane model seems to be in good agreement with spectroscopic EPR/ENDOR data,[4] and both are in qualitative agreement with the arrangement of the Mn atoms in the recently reported crystal structure of PSII in *Synechococcus elongatus* at the level of 3.8 Å resolution.[5] The OEC is known to undergo a series of one-electron photoredox processes[6] through states labeled $S_0$ to $S_4$ (Scheme 1) in which the oxidation states of only two of the four Mn atoms in the cluster are affected.[7] When the $S_4$ state is reached, $O_2$ is released, and the system spontaneously returns to its lowest oxidation state $S_0$ thus completing the catalytic cycle.

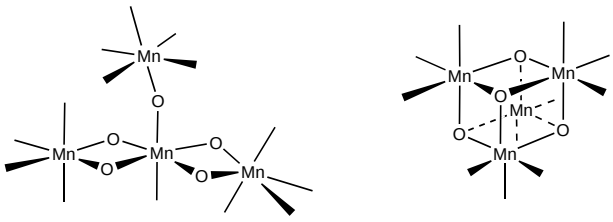


**1**

There are no structural data for the $S_4$ state, since it has not been trapped or otherwise detected. Furthermore, the way in which two oxygen atoms couple to form a dioxygen molecule, thus taking the $S_4$ back to the $S_0$ state to complete the catalytic cycle, is still unclear. It has been proposed that the evolution of oxygen in the $S_3 \rightarrow S_4 \rightarrow S_0$ steps results from a nucleophilic attack[8] of an $OH^-$ on a terminal oxo ligand attached to a Mn atom in the +5 oxidation state. We notice, however, that a terminal oxo ligand attached to a $Mn^V$ has been well characterized and is stable,[9–11] and that the permanganate ion does not generate oxygen in water even if oxo ligands are bonded to a $Mn^{VII}$ ion. Hence, there is no experimental evidence to support such a mechanism.

[a] Prof. Dr. S. Alvarez, Dr. G. Aullón, Dr. E. Ruiz
Departament de Química Inorgànica and
Centre de Recerca en Química Teòrica
Universitat de Barcelona, Diagonal 647, 08028 Barcelona (Spain)
Fax: (+34) 93-490 7725
E-mail: santiago.alvarez@qi.ub.es

  0947-6539/02/0811-2508 $ 20.00+.50/0 

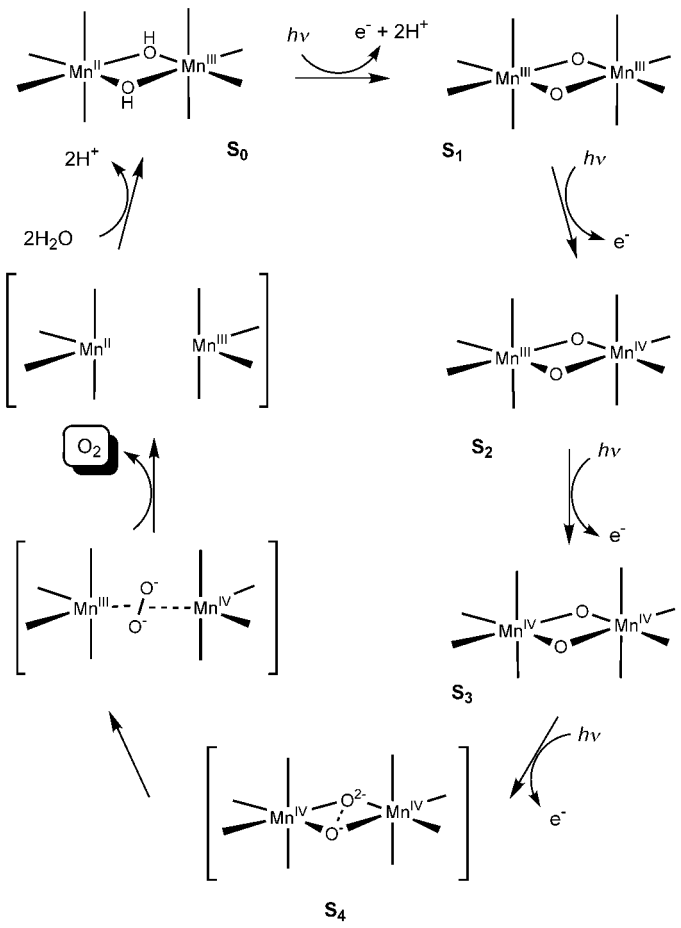


Scheme 1. $S_0$ to $S_4$ steps of the photocatalytic cycle in the oxygen-evolving complex of PS II (only a dinuclear unit of the tetranuclear manganese complex is shown), together with intramolecular one-electron transfer steps leading from $S_4$ to $S_0$ (in square brackets) according to the model calculations reported here.

**Abstract in Spanish:** *El mecanismo de formación de una molécula de dioxígeno en el complejo generador de oxígeno (OEC) del fotosistema II (PS II) constituye una etapa crucial de la fotosíntesis y es aun objeto de debate. La unidad más sencilla presente en el OEC capaz de producir $O_2$ es un complejo dinuclear de manganeso con puentes oxo, que forma parte de una agrupación tetranuclear $Mn_4$. En este artículo se presenta un estudio teórico de los modelos $[Mn_2(\mu\text{-}O)_2(NH_3)_6(H_2O)_2]^{n+}$ ($n=2-5$), para los que se han realizado cálculos del funcional de la densidad con varias configuraciones electrónicas. La descripción de orbitales moleculares que se deduce de los cálculos sugiere que la oxidación del complejo $Mn_2^{IV,IV}/(O^{2-})_2$ afecta particularmente a los átomos de oxígeno, descartándose la existencia de un estado de oxidación $Mn^V$, al tiempo que la formación de un enlace incipiente O–O en la especie transitoria $O_2^{3-}$ evoluciona exotérmicamente hacia la disociación de oxígeno y la formación de una pareja de complejos con estados de oxidación $Mn_2^{II,III}$. Estos resultados identifican las características electrónicas que serían necesarias para permitir un mecanismo intramolecular de formación de un enlace oxígeno–oxígeno en el OEC durante la fotosíntesis.*

An alternative intramolecular pathway[12] implies coupling of the oxo bridges across a $Mn_2O_2$ face of a cubane. This mechanism has attracted renewed interest recently due to the report of dioxygen evolution from synthetic $Mn_4O_4$ cubanes, which had been demonstrated to proceed in this way.[13, 14] Oxygen has also been reported to evolve upon chemical oxidation of a dinuclear Mn complex,[15, 16] although the origin of the oxygen molecule formed is still a matter of controversy.[17]

In spite of the lack of precise structural information about the $Mn_4$ cluster in the different states of PS II, a common motif in all the models proposed is a bisoxo-bridged dinuclear Mn unit. For this reason, several theoretical studies on dinuclear molecular models have been reported.[18–21] In the only theoretical study that analyzed the intramolecular mechanism, based on semiempirical calculations,[19] this route was ruled out by the high energy barrier found at the computational level used. In an otherwise detailed density functional study of model dinuclear complexes, only oxidation states up to $Mn_2^{IV,IV}$ were considered, without geometry optimizations.[21] Other work focused on the oxygen-radical mechanism, in which terminal oxo ligands are involved in the formation of the dioxygen molecule. In one case,[18] the presence of terminal oxo groups attached to the two Mn atoms in neighboring positions was assumed, a feature that is absent in the recently reported synthetic models.[8, 13] Furthermore, the proposed mechanism requires two two-electron oxidations of a $Mn_2^{IV,IV}$ pair; this is an unrealistic model of the $S_3 \rightarrow S_4 \rightarrow S_0$ steps in the OEC. Another recent study[20] also focused on an oxygen radical mechanism, but neither the $S_4$ state nor the $S_4 \rightarrow S_0$ step was studied in detail.

In previous theoretical studies of the delocalized bonding in the $M_2X_2$ rings of doubly bridged dinuclear complexes,[22–24] we found that such rings are quite efficient in transferring electrons from the skeleton to the transition metals and vice versa. For the case of oxo-bridged compounds, the displacement of the equilibrium toward the oxo complex or the formation of a peroxo group has been shown to depend on a variety of subtle factors, such as steric[25, 26] or solvent effects[27] or the relative electronegativities of the metal and bridging atoms.[28] Hence, it seemed natural to us that the $Mn_2O_2$ ring in an oxo-bridged dinuclear complex could form an intramolecular O–O bond, and we decided to explore such possibility theoretically using a simplified model complex, $[Mn_2(\mu\text{-}O)_2(NH_3)_6(H_2O)_2]^{n+}$ and modern density functional calculations. The simple ligands adopted in this model are expected to reproduce the main trends of the electronic structure and bonding in more complex systems, as recently shown for a dinuclear model of manganese catalase.[29] The possibility of intramolecular oxygen–oxygen bond formation can be thus evaluated based on fundamental characteristics, namely the formal oxidation state of the cluster and the topology of the two edge-sharing octahedra with a central $Mn_2O_2$ core.

## Computational Details

All calculations were carried out with the help of the Gaussian94 program[30] by using a LANL2DZ double-ζ basis set and the hybrid

B3LYP method.[31, 32] In previous studies[33–35] we have shown that this method provides excellent results for evaluating the relative energies of several spin states in dinuclear complexes. A $C_{2h}$ molecular symmetry was adopted for the heavy atoms' skeleton in the calculations. The coordinated water molecules in the model compounds $[Mn_2(\mu\text{-}O)_2(NH_3)_6(H_2O)_2]^{n+}$ occupy *trans* positions coplanar with the $Mn_2O_2$ framework. For each case studied, different electron configurations were analyzed to take into account: 1) local high- and low-spin states at each Mn atom, 2) ferro- or antiferromagnetic alignment of the local spins, and 3) localized and delocalized states for the mixed-valence compounds.

The potential energy surface of the $Mn_2^{IV,V}$ complex reported here was shown to be unbiased by the computational approach used in several ways: 1) calculations were repeated without any symmetry restrictions; 2) calculations were also performed considering the effect of a dielectric environment; 3) the charge of the complex was artificially lowered by decreasing the nuclear charge at each Mn atom by 0.5 to make sure that the results were not biased by the increased charge of $Mn_2^{IV,V}$ relative to $Mn_2^{IV,IV}$; 4) calculations with a triple-$\zeta$ basis set were performed for the $Mn_2^{IV,IV}$ and $Mn_2^{IV,V}$ oxidation states and no significant differences were found. To simulate the dielectric environment of the charged species studied, we used the nonequilibrium implementation of the polarizable continuum model in its conductor version (CPCM)[36, 37] with the dielectric constant of water (78.39). The oxidation states and formal charges presented in Figure 5, below, correspond to the most stable electron configuration for each of 133 geometries explored along the reaction path. They were determined from the occupation of metal d and oxygen $\pi^*$ and $\sigma^*$ orbitals and checked for consistency with the Mulliken net charges and spin densities.

## Results and Discussion

**Electronic structures of the $Mn_2^{III,III}$, $Mn_2^{III,IV}$ and $Mn_2^{IV,IV}$ complexes**: The $[Mn_2(\mu\text{-}O)_2(NH_3)_6(H_2O)_2]^{n+}$ $(n = 2, 3, 4)$ complexes constitute our theoretical models for the redox-active dinuclear unit in the $S_1$ to $S_3$ states of the OEC, respectively. Local high- and low-spin electron configurations at each Mn atom (indicated by the occupation of the $t_{2g}$-like and $e_g$-like d orbitals in the approximately octahedral ligand environment) have been considered. Furthermore, states with ferro- (parallel spins) and antiferromagnetic (antiparallel spins) exchange coupling of the unpaired electrons at each Mn atom were also evaluated.[38,35] The results of our calculations for the different electron configurations explored are summarized in Table 1.

The description of the electronic and molecular structures of the model complexes obtained from the calculations is in good agreement with experimental data for $Mn_2^{III,III}$, $Mn_2^{III,IV}$ and $Mn_2^{IV,IV}$ complexes (Tables 2, 3, and 4), in regard to: 1) the formal oxidation states of the Mn atoms; 2) the local high-spin configuration at each Mn atom;[39] 3) the antiferromagnetic nature and the magnitude of the exchange coupling[40,41] between the two Mn atoms (negative $J$ values); 4) the electron spin resonance (ESR) spectra;[39] 5) the bridging Mn–O lengths;[7, 15, 42] 6) the asymmetry of the $Mn_2^{III,IV}$ complex; 7) the Mn–Mn distance, and 8) the nonbonding oxygen – oxygen distances, which are larger than 2.28 Å in all the

Table 2. Experimental bond lengths [Å], exchange coupling constants [$cm^{-1}$], and CCDC reference codes for $Mn_2^{III,III}$ dinuclear complexes.

| Ref. | Mn–Mn | O···O | Mn–O[a] | $J$ | Donor Set |
|---|---|---|---|---|---|
| HEWJIC | 2.699 | 2.526 | 1.848 | – 201 | $N_4$ |
| KAWLID | 2.676 | 2.526 | 1.840 (13) | | $N_4$ |
| KAWLID10 | 2.676 | 2.526 | 1.840 (13) | – 173 | $N_4$ |
| VEZHIR | 2.685 | 2.521 | 1.842 (20) | | $N_4$ |
| VEZHOX | 2.674 | 2.500 | 1.830 | | $N_4$ |

[a] Standard deviation (sd) for Mn–O bond lengths shown in parenthesis for asymmetric complexes. Statistics for five crystallographically independent data sets in four compounds (range/mean/estimated standard deviation): 2.67 – 2.70/2.682/10, 2.50 – 2.53/2.520/11, 1.83 – 1.85/1.840/6 for the Mn–Mn, O···O and Mn–O lengths, respectively.

Table 1. Calculated data for model complexes $[Mn_2(\mu\text{-}O)_2(NH_3)_6(H_2O)_2]^{n+}$ in their most stable electron configurations.

| electronic structure | | distances [Å][c] | | | Energy[d] | $J$ |
|---|---|---|---|---|---|---|
| $S$[a] | local conf.[b] | Mn–Mn | O–O | Mn–O | [kcal mol$^{-1}$] | [$cm^{-1}$] |
| $Mn_2^{II,III}$, $n = 1$ ($S_0$) | | | | | | |
| 1/2 | $t_{2g}^3e_g^2/t_{2g}^3e_g^1$ | 2.833 | 2.635 | 1.813, 2.063 | 0.0 | – 45 |
| 9/2 | $t_{2g}^3e_g^2/t_{2g}^3e_g^1$ | 2.843 | 2.644 | 1.813, 2.077 | 1.5 | |
| 9/2[f] | $t_{2g}^3e_g^{1.5}$ | 2.767 | 2.720 | 1.940 | 7.3 | |
| $Mn_2^{III,III}$, $n = 2$ ($S_1$) | | | | | | |
| 0[e] | $t_{2g}^3e_g^1$ | 2.791 | 2.433 | 1.852 | 0.0 | – 177 |
| 4 | $t_{2g}^3e_g^1$ | 2.810 | 2.452 | 1.865 | 5.0 | |
| 0[e] | $t_{2g}^4$ | 2.845 | 2.423 | 1.869 | 43.3 | |
| 2 | $t_{2g}^4$ | 2.802 | 2.459 | 1.864 | 41.9 | |
| exp.[c] | | 2.67 – 2.70 | 2.50 – 2.53 | 1.83 – 1.85 | | – 187 ± 14 |
| $Mn_2^{III,IV}$, $n = 3$ ($S_2$) | | | | | | |
| 1/2[e] | $t_{2g}^3e_g^1/t_{2g}^3$ | 2.845 | 2.358 | 1.777, 1.921 | 0.0 | – 236 |
| 7/2 | $t_{2g}^3e_g^1/t_{2g}^3$ | 2.845 | 2.397 | 1.793, 1.928 | 5.1 | |
| 7/2[f] | $t_{2g}^3e_g^{0.5}$ | 2.871 | 2.392 | 1.869 | 13.4 | |
| 1/2[e] | $t_{2g}^4/t_{2g}^3$ | 2.859 | 2.350 | 1.776, 1.927 | 16.3 | |
| 5/2 | $t_{2g}^4/t_{2g}^3$ | 2.818 | 2.398 | 1.783, 1.918 | 16.5 | |
| 5/2[f] | $t_{2g}^{3.5}$ | 2.794 | 2.390 | 1.838 | 18.3 | |
| exp.[c] | | 2.55 – 2.74 | | 1.77 – 1.81<br>1.81 – 1.89 | | – 265 ± 63 |
| $Mn_2^{IV,IV}$, $n = 4$ ($S_3$) | | | | | | |
| 0[e] | $t_{2g}^3$ | 2.902 | 2.283 | 1.846 | 0.0 | – 201 |
| 3 | $t_{2g}^3$ | 2.941 | 2.318 | 1.873 | 3.4 | |
| exp.[c] | | 2.57 – 2.78 | 2.25 – 2.54 | 1.77 – 1.83 | | – 186 ± 108 |

[a] Total spin. [b] Occupation of the Mn 3d orbitals, labeled according to octahedral symmetry. [c] Ranges of experimental values; distances for di-$\mu$-oxo complexes have been obtained from the Cambridge Structural Database (see Tables 2 – 4). [d] Relative to the ground state. [e] Broken symmetry solution. [f] Delocalized mixed-valence state.



0947-6539/02/0811-2510 $ 20.00+.50/0 *Chem. Eur. J.* **2002**, *8*, No. 11

Table 3. Experimental bond lengths [Å], exchange coupling constants [$cm^{-1}$] and CCDC reference codes for $Mn_2^{III,IV}$ dinuclear complexes.

| Ref. | Mn–Mn | O···O | Mn–O[a] | *J* | Donor Set |
|---|---|---|---|---|---|
| FEBKUS | 2.698 | 2.431 | 1.816 | –268, –296 | $N_4$ |
| FEBKUS01 | 2.695 | 2.426 | 1.813 | –296 | $N_4$ |
| FERZUX | 2.588 | 2.499 | 1.812 | –440 | $N_3O_{ax}$ |
| FIQFIU | 2.733 | 2.373 | 1.810 | | $N_3O_{eq}$ |
| FIQFIU | 2.724 | 2.389 | 1.812 | | $N_3O_{eq}$ |
| FIQFIU01 | 2.731 | 2.391 | 1.815 | | $N_3O_{eq}$ |
| FIQFIU01 | 2.733 | 2.383 | 1.813 | | $N_3O_{eq}$ |
| FOGHAK | 2.659 | 2.467 | 1.814 (39) | –280 | $N_4$ |
| GAMFEF | 2.679 | 2.437 | 1.811 (76) | –292 | $N_4$ |
| GAVWIJ | 2.667 | 2.437 | 1.817 (36) | –228 | $N_2Cl_{eq}O_{ax}$ |
| GEPSUP | 2.643 | 2.464 | 1.807 (60) | –318 | $N_4$ |
| GIXKON | 2.646 | 2.472 | 1.811 (52) | –316 | $N_4$ |
| HEWJEY | 2.679 | 2.471 | 1.822 (55) | –320 | $N_4$ |
| HEWJOI | 2.692 | 2.466 | 1.826 (63) | –293 | $N_4$ |
| HIRMEA | 2.719 | 2.402 | 1.814 | –300 | $N_4$ |
| JITXUF | 2.654 | 2.462 | 1.810 (39) | –202 | $N_3O_{ax}$ |
| KEVRUY | 2.723 | 2.453 | 1.833 | | $N_3O_{eq}$ |
| KEZKUV | 2.731 | 2.411 | 1.821 | –237 | $N_4$ |
| KEZLAC | 2.728 | 2.406 | 1.819 | | $N_4$ |
| KEZLAC | 2.736 | 2.419 | 1.826 | | $N_4$ |
| KUVPIA | 2.628 | 2.453 | 1.814 (48) | –234 | $N_2O_2/N_3O_{ax}$ |
| QABGUV | 2.573 | 2.515 | 1.810 (7) | –224 | $N_3O_{ax}$ |
| QABHAC | 2.553 | 2.525 | 1.806 (49) | –220 | $N_3O_{ax}$ |
| SAHZAC | 2.622 | 2.431 | 1.797 (42) | –288 | $N_3O_{ax}$ |
| SAWYEU | 2.704 | 2.410 | 1.811 (47) | | $N_4$ |
| SEJXUA | 2.741 | 2.407 | 1.824 (36) | | $N_4$ |
| SIBZUY | 2.693 | 2.424 | 1.812 | | $N_4$ |
| SIBZUY | 2.691 | 2.435 | 1.814 | | $N_4$ |
| VUBGAA | 2.591 | 2.491 | 1.808 (49) | –250 | $N_3O_{ax}$ |
| WABFIO | 2.695 | 2.440 | 1.818 | | $N_4$ |
| YEMCIC | 2.711 | 2.403 | 1.812 (73) | | $N_4$ |
| YEXLOC10 | 2.644 | 2.465 | 1.809 (49) | –291 | $N_3O_{ax}$ |
| YEXLOC10 | 2.651 | 2.479 | 1.817 (63) | –291 | $N_3O_{ax}$ |
| ZAXNER | 2.705 | 2.517 | 1.848 (76) | –300 | $N_4$ |
| ZEQGEH | 2.633 | 2.461 | 1.816 (69) | –328 | $N_3O_{ax}$ |
| ZUKHES | 2.677 | 2.466 | 1.821 (94) | –278 | $N_4$ |

[a] Standard deviation for Mn–O bond lengths shown in parenthesis for asymmetric complexes. Statistics for 36 crystallographically independent data sets in 28 compounds (range/mean/esd): 2.55–2.74/2.677/50, 2.37–2.52/2.444/39, 1.80–1.85/1.816/9 for the Mn–Mn, O···O and Mn–O lengths, respectively. Mn–O bonds in 21 crystallographically independent asymmetric molecules in 20 compounds (range/mean/esd): short: 1.77–1.81/1.788/11, long: 1.81–1.89/1.842/16.

Table 4. Experimental bond distances [Å], exchange coupling constants *J* [$cm^{-1}$] and CCDC reference codes for $Mn_2^{IV,IV}$ dinuclear complexes.

| Ref. | Mn–Mn | O···O | Mn–O | *J* | Donor set |
|---|---|---|---|---|---|
| FEBKOM | 2.745 | 2.325 | 1.799 (3) | –288 | $N_4$ |
| HAJZOH | 2.642 | 2.391 | 1.794 (2) | –134 | $N_2O_{eq},O_{ax}$ |
| HAJZOH01 | 2.640 | 2.402 | 1.797 (4) | –87 | $N_2O_{eq}O_{ax}$ |
| HALGEG | 2.737 | 2.396 | 1.819 | | $N_2O_{eq}O_{ax}$ |
| HIMQAV | 2.625 | 2.446 | 1.805 (8) | | $N_3O_{ax}$ |
| HISGOF | 2.722 | 2.378 | 1.807 | –195 | $N_3O_{eq}$ |
| JATLEV | 2.736 | 2.348 | 1.803 | | $N_2O_{2eq}$ |
| JAVYEK | 2.746 | 2.386 | 1.819 | –173 | $N_2O_{2eq}$ |
| JEBXUJ | 2.681 | 2.430 | 1.819 (4) | –171 | $N_2Cl_{eq}O_{ax}$ |
| JEWNII | 2.679 | 2.393 | 1.806 (20) | –182 | $N_2O_{eq}O_{ax}$ |
| JIWVUG | 2.702 | 2.382 | 1.810 (3) | –79 | $N_2O_{eq}O_{ax}$ |
| JIWWAN | 2.700 | 2.371 | 1.808 (17) | –79 | $N_2O_{eq}O_{ax}$ |
| JOJQUU | 2.568 | 2.530 | 1.802 | | $N_4$ |
| KEGNUF | 2.671 | 2.444 | 1.810 | –251 | $N_4$ |
| LIDVUP | 2.760 | 2.414 | 1.834 (2) | –268 | $N_2O_{eq}O_{ax}$ |
| LIDVUP | 2.746 | 2.349 | 1.807 (119) | –176 | $N_4/N_2O_{eq}O_{ax}$ |
| LIDVUP | 2.735 | 2.428 | 1.830 (101) | –176 | $N_4/N_2O_{eq}O_{ax}$ |
| NANNIZ | 2.715 | 2.386 | 1.807 | –160 | $N_2O_{2eq}$ |
| PALJOB | 2.580 | 2.484 | 1.799 (9) | –248 | $N_3O_{ax}$ |
| PALJOI | 2.596 | 2.499 | 1.814 (2) | –152 | $N_3O_{ax}$ |
| POKQUB | 2.707 | 2.425 | 1.817 | –160 | $N_2O_{2eq}$ |
| POKRAI | 2.733 | 2.393 | 1.816 | –176 | $N_2O_{eq}O_{ax}$ |
| QABHEG | 2.599 | 2.442 | 1.797 | –200 | $N_3O_{ax}$ |
| ROLJEH | 2.780 | 2.345 | 1.818 (2) | | $N_2O_{2eq}$ |
| SICBAH | 2.746 | 2.246 | 1.774 | –262 | $N_4$ |
| SONLIQ | 2.631 | 2.453 | 1.799 | –158 | $N_2O_{2eq}$ |
| SOZMUP | 2.728 | 2.405 | 1.818 | –164 | $N_2O_{eq}O_{ax}$ |
| SOZMUP01 | 2.731 | 2.387 | 1.814 | –164 | $N_2O_{eq}O_{ax}$ |
| SOZVEI | 2.718 | 2.369 | 1.803 (4) | –248, –211 | $N_4$ |
| TOFQOU | 2.688 | 2.391 | 1.799 | | $N_2O_{2eq}$ |
| TORSOI | 2.718 | 2.407 | 1.816 | | $N_2O_{2eq}$ |
| TORSOI01 | 2.718 | 2.407 | 1.816 | –160 | $N_2O_{2eq}$ |
| TORSUO | 2.729 | 2.416 | 1.822 | | $N_2O_{eq}O_{ax}$ |
| TORSUO01 | 2.729 | 2.416 | 1.822 | –156 | $N_2O_{eq}O_{ax}$ |
| VADCOS | 2.626 | 2.538 | 1.826 | | $N_3O_{ax}$ |
| WADKUH | 2.591 | 2.454 | 1.797 (6) | | $N_3O_{ax}$ |
| WADKUH | 2.591 | 2.459 | 1.798 (6) | | $N_3O_{ax}$ |
| WADLAO | 2.625 | 2.468 | 1.816 (10) | | $N_3O_{ax}$ |
| ZEQGIL | 2.745 | 2.347 | 1.806 | | $N_3F_{eq}$ |
| ZEQGOR | 2.756 | 2.347 | 1.810 | –294 | $N_3Cl_{eq}$ |
| ZUVPUB | 2.675 | 2.392 | 1.807 (5) | | $N_2O_{eq}O_{ax}$ |

Statistics for 41 crystallographically independent data sets in 34 compounds (range/mean/esd): 2.57–2.78/2.690/59, 2.25–2.54/2.407/55, 1.77–1.83/1.809/11 for the Mn–Mn, O···O and Mn–O lengths, respectively.

cases (Table 1). The ability of our model calculations to reproduce the structure and properties of the well-characterized synthetic models makes us confident that a similar theoretical study should offer a sensible description of the electronic structure of the ill-characterized species produced by a one-electron oxidation of a $Mn_2^{IV,IV}$ complex.

**Oxygen evolution from an orbital point of view**: We have theoretically simulated the $S_3$ to $S_4$ oxidation through calculations on the $[Mn_2(\mu\text{-}O)_2(NH_3)_6(H_2O)_2]^{5+}$ model in its lowest spin state ($S = ½$), produced by removing an electron from the $Mn_2^{IV,IV}$ complex. The results of such calculations may best be understood if a qualitative molecular orbital description, based on the calculated Kohn–Sham orbitals, is presented first (Figure 1). The main points of our analysis are as follows:

1) In the formal $Mn_2^{IV,IV}$ oxidation state, the metal $d(t_{2g})$ orbitals are strongly stabilized due to the large effective nuclear charge of the metal atoms, and the HOMO is a Mn–O bonding orbital ($b_{3u}$ in Figure 1, left) with a significant contribution from the oxygen atoms.
2) Oxidation of the $Mn_2^{IV,IV}$ complex thus removes an electron from the HOMO ($b_{3u}$ in Figure 1, column I); this results in formal oxidation states $Mn_2^{IV,IV}$ and $O_2^{3-}$ (column II) rather than $Mn_2^{IV,V}$ and $O^{2-}$.
3) Given the O–O σ-antibonding character of the $b_{3u}$ orbital, the removal of one electron favors the approach of the two bridging atoms (i.e., an incipient formation of the O–O bond across the $Mn_2O_2$ ring).
4) As the two oxygen atoms approach each other, $b_{3u}$ is strongly destabilized until a crossing with the $d_{x^2-y^2}$ ($2b_{3u}$ and $2b_{2g}$) orbitals occurs (labeled *a* in Figure 1)—actually an avoided crossing in the case of $2b_{3u}$ as required by symmetry.
5) The resulting electron configuration (column III) with an empty $\sigma^*_{O\text{-}O}$ orbital ($b_{3u}$) indicates the formation of a

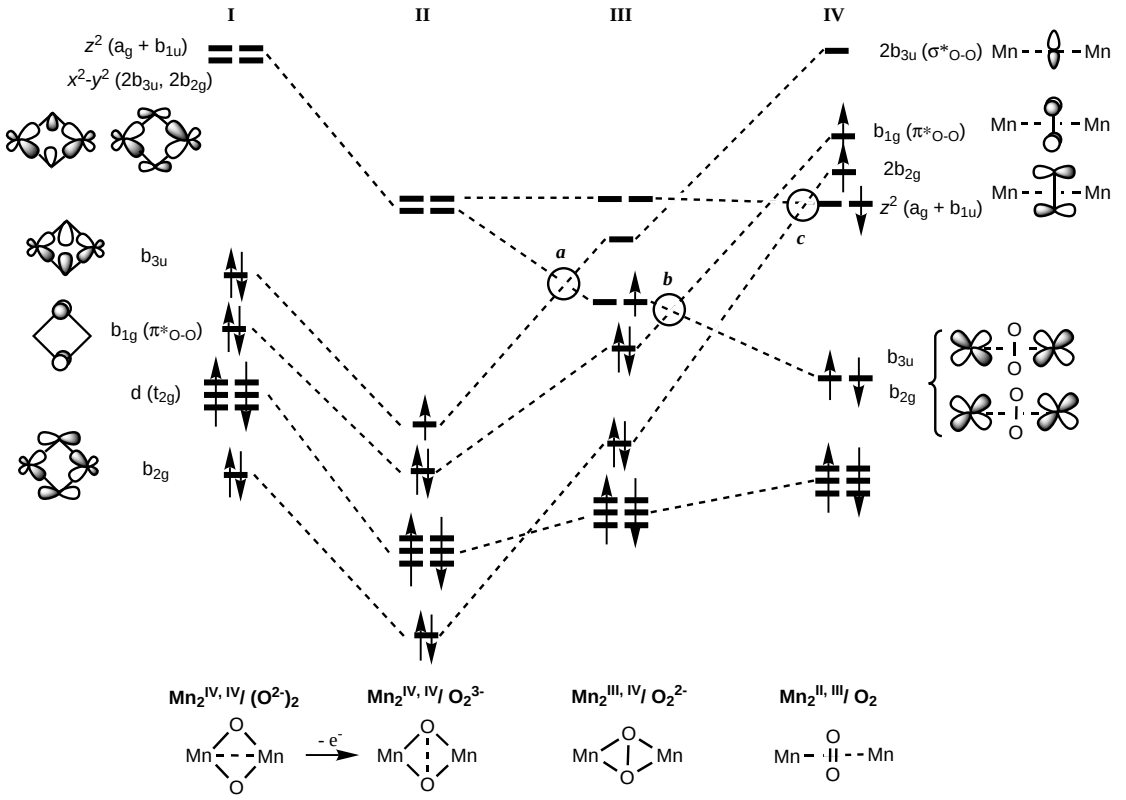


Figure 1. Comparison of the energies and composition of the most relevant molecular orbitals of $[Mn_2(\mu\text{-}O)_2(NH_3)_6(H_2O)_2]^{n+}$ for $n = 4$ (column I) and $n = 5$ at different Mn–O distances (columns II – IV, O–O distance optimized in each case and the rest of the molecule frozen with the same geometry as in I), deduced from analysis of the Kohn – Sham orbitals. The Mn–O distances used and the resulting charge distributions for $n = 5$ are as follows: 1.85 Å, $Mn_2^{IV,IV}/O_2^{3-}$ (column II); 2.05 Å, $Mn_2^{III,IV}/O_2^{2-}$ (column III); 2.5 Å, $Mn_2^{III,III}/O_2^{-}$ (not shown), and 3.0 Å, $Mn_2^{II,III}/O_2$ (column IV). The $\alpha$ and $\beta$ spin orbitals obtained from unrestricted calculations are drawn at the same energy for simplicity.

peroxo ($O_2^{2-}$) bridging group combined with the $Mn_2^{III,IV}$ oxidation states.

6) Emptying the $b_{3u}$ bonding orbital of the $Mn_2O_2$ ring induces an elongation of the Mn–O bonds; this in turn stabilizes the two combinations of $e_g$-type orbitals (now $b_{3u}$ and $2b_{2g}$).
7) As the O–O distance continues to decrease, the $b_{1g}$ and $b_{2g}$ orbitals are progressively destabilized due to their $\pi^*_{O-O}$ antibonding character; this results in orbital crossings (labeled *b* and *c* in Figure 1) that take the system to the $Mn_2^{III,III}/O_2^{-}$ (not shown) and $Mn_2^{II,III}/O_2$ configurations (column IV).
8) In the last state, given the similar energies of $b_{1g}$, $b_{2g}$, and $d_{z^2}$ orbitals, the resulting electron configuration presents half occupied $\pi^*_{O-O}$ orbitals, as in the ground state of the free dioxygen molecule, combined with antiferromagnetically coupled high-spin $Mn^{II}$ and $Mn^{III}$ ions; this is consistent with a $Mn_2^{II,III}$/dioxygen description of the system.
9) Accompanying the ring squeezing, there is a progressive localization of the molecular orbitals.[33] In the $Mn_2^{IV,IV}$/oxo species, $b_{3u}$ and $b_{2g}$ are delocalized (Mn–O bonding) molecular orbitals, $2b_{3u}$ and $2b_{2g}$ are their antibonding counterparts (column I); whereas in the $Mn_2^{II,III}$/dioxygen case (column IV) $b_{3u}$ and $b_{2g}$ are localized on the Mn atoms, and $2b_{3u}$ and $2b_{2g}$ are localized on the oxygen atoms (namely the $\sigma^*$ and $\pi^*$ orbitals of the dioxygen molecule). This is shown schematically in Figure 2 for the case of the $b_{3u}$ orbitals.
10) Although the orbitals shown in Figure 1 increase in energy upon formation of the dioxygen molecule, the overall process is favored by the stabilization of the low-lying occupied oxygen – oxygen $\sigma$ and $\pi$ bonding molecular orbitals (not shown for simplicity).

Orbital evolution during the oxygen-generation step determines a barrierless process in our calculations once the

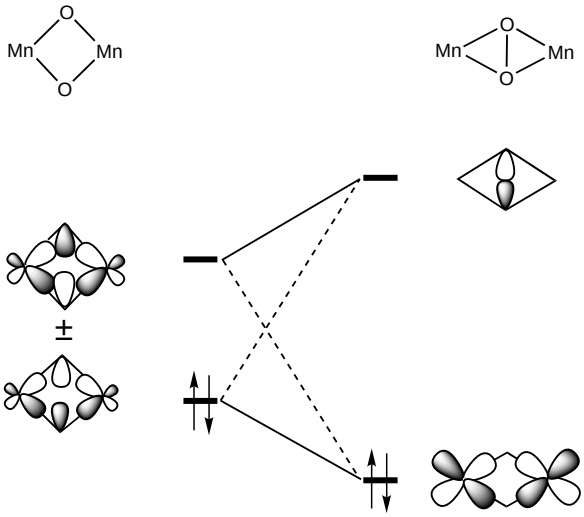


Figure 2. Transition of molecular orbital $b_{3u}$ from delocalized to localized on the Mn atoms.



0947-6539/02/0811-2512 $ 20.00+.50/0 *Chem. Eur. J.* **2002**, *8*, No. 11

$Mn_2^{IV,IV}$ couple is oxidized (see below) and clearly shows that oxygen–oxygen bond formation is determined by the overall oxidation state, the molecular topology, and the symmetry of the $Mn_2O_2$ framework. We note that a similar orbital analysis was previously presented by Proserpio, Hoffmann, and Dismukes;[19] based on extended Hückel (EH) calculations. However, these authors found a high energy barrier for the intramolecular pathway; this has made most researchers disregard it as a feasible mechanism for the oxygen-evolving step in PS II. Since the work of Proserpio et al. gave a similar orbital picture to the one described here, the main quantitative difference with our results is the evaluation of the energy barrier and it is worth discussing the reasons for the different results.

First, the study on the intramolecular oxygen coupling in the work by Proserpio et al. was done for a system with one less electron, that is, $Mn_2^{IV,IV}$, a system for which our DFT calculations indicate that the oxo-bridged conformation is more stable than the peroxo form by 26 kcal · mol$^{-1}$. Second, the Mn–O lengths were kept constant in the EH calculations (because the energy dependence on bond lengths is not well evaluated by that method), whereas our more detailed orbital analysis (and the results of our calculations, see below) clearly show that an important Mn–O bond elongation is required to form the O–O bond. Third, a typical approximation used in extended Hückel calculations consists of keeping the energies of the atomic orbitals constant within a series of calculations, as indeed made by Proserpio et al., independent of the oxidation state of the metal. Therefore, the important decrease in the d-orbital energies when the oxidation state of Mn goes from +2 to +5 that we found in the DFT calculations was not taken into account by these authors. The effect of the net atomic charge on the 3d-orbital energies of Mn used in charge-iterated EH calculations,[43] as obtained from experimental ionization energies, is illustrated in Figure 3. The parameters used by Proserpio et al. correspond to a net charge of +0.3 (indicated by an arrow) and have the manganese 3d orbitals above the oxygen 2p ones. But increasing the Mn net charge above +0.5 reverses the situation, as found in our DFT calculations for the higher oxidation states of Mn. It was clearly shown by Proserpio et al. that the calculated energy barrier resulted from the need of

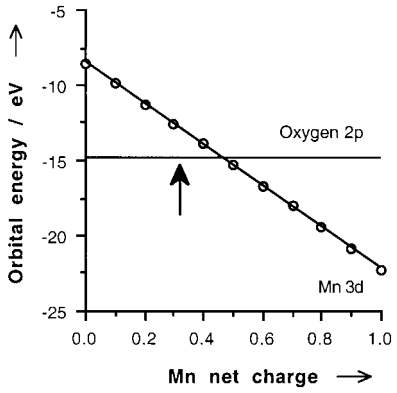


Figure 3. Energy of the Mn 3d orbital as a function of the atomic charge,[43] relative to the oxygen 2p orbital energy. The values used by Proserpio et al. in previous extended Hückel calculations are indicated by an arrow.

σ*(O–O) to cross the $t_{2g}$ orbitals, so the height of the EH barrier is dependent on the parametrization chosen for the Mn 3d orbitals. In summary, the high energy barrier found by Proserpio et al. for the intramolecular oxygen-generation pathway stems from the oxidation states chosen together with the use of the standard parametrization of the energies of the Mn 3d orbitals in the EH calculations, which results in an inverted-energy ordering of the $d(t_{2g})$ and $b_{3u}$ orbitals with respect to the present DFT calculations.

**The oxygen evolution step: computational results**: Upon one-electron oxidation of the oxo-bridged $Mn_2^{IV,IV}$ dinuclear complex with a frozen geometry, the resulting electron configuration corresponds to a $Mn_2^{IV,IV}/O_2^{3-}$ species. We have been able to calculate the wave function corresponding to the $Mn_2^{IV,V}/(O^{2-})_2$ charge distribution for the same geometry, but it is clearly at higher energy (29 kcal · mol$^{-1}$). These results are just a reflection of the orbital picture described above, and indicate that the $Mn^V$ oxidation state cannot be attained within a $Mn_2O_2$ ring. If the oxygen–oxygen distance is reoptimized after oxidation, keeping the Mn–O bond lengths unchanged, an energy minimum appears at 2.0 Å (Figure 4,

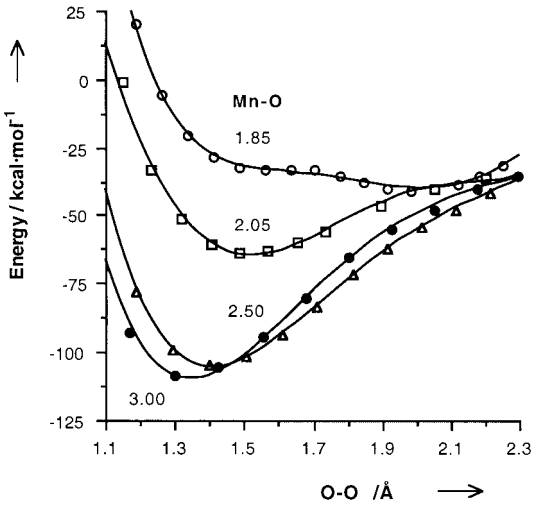


Figure 4. Energy of $[Mn_2(\mu\text{-}O)_2(NH_3)_6(H_2O)_2]^{5+}$ as a function of the O–O distance at different values of the bridging Mn–O bond length, with the rest of the molecule frozen at the optimized geometry of the complex with one more electron. The electron configurations at the minima correspond to the $Mn_2^{IV,IV}/O_2^{3-}$ (○), $Mn_2^{III,IV}/(O_2^{2-})$ (□), $Mn_2^{III,III}/(O_2^{-})$ (△), and $Mn_2^{II,III}/(O_2)$ (●) oxidation states (for Mn–O = 1.85, 2.05, 2.50, and 3.00 Å, respectively). All energies are relative to that calculated for the $Mn_2^{IV,V}/(O^{2-})_2$ state.

○). If, however, the Mn–O bond length is increased and the geometry of the central $Mn_2O_2$ core reoptimized, the energy of the system decreases, and the minimum is shifted to shorter O–O distances. Extrapolation of the trends found in Figure 4 predicts cleavage of the Mn–O bonds and formation of an O–O bond. This is actually found in our calculations when full geometry optimization of $[Mn_2(\mu\text{-}O)_2(NH_3)_6(H_2O)_2]^{5+}$ in the gas phase is performed, and leads to the formation of a dioxygen molecule and its dissociation from the two resulting mononuclear complexes. If the effect of a dielectric environment is incorporated into the calculations, the same trend remains: the energy of the system is lowered by about

9 kcal mol$^{-1}$ upon shortening the O–O distance from 1.99 to 1.42 Å and correspondingly increasing the Mn–O lengths from 1.85 to 2.50 Å.

As the $Mn_2O_2$ core dissociates, the changes in electronic configuration are consistent with an electron drift from the O to the Mn atoms, as in the orbital model discussed above. A map of the charge distribution within the $Mn_2O_2$ core as a function of the Mn–O and O–O lengths is presented in Figure 5. Four regions can be identified, which correspond to

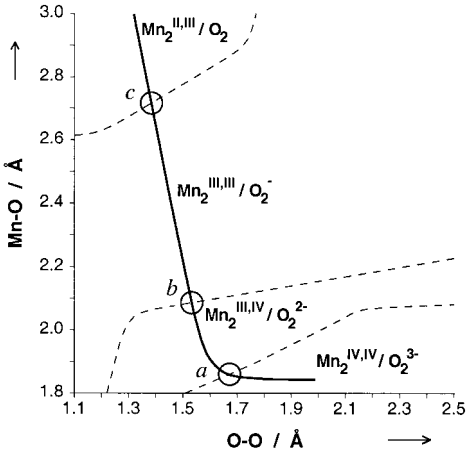


Figure 5. Map of the calculated oxidation states of $[Mn_2(\mu\text{-}O)_2(NH_3)_6(H_2O)_2]^{5+}$ as a function of the O–O and bridging Mn–O distances. The thick line represents the path of least energy. The regions corresponding to different electron distributions have been deduced from calculations for 133 geometries with different Mn–O and O–O separations, but the rest of the molecule kept frozen at the optimized geometry of the $Mn_2^{IV,IV}/(O^{2-})_2$ complex. The points marked with circles correspond to the orbital crossings indicated in Figure 1.

decreasing oxidation states of the $Mn_2$ pair combined with decreasing negative charge at the oxygen atoms (from bottom right to top left) in one-electron steps that smoothly accompany the changes in bond lengths of the $Mn_2O_2$ framework. These one-electron transfer steps (circled) correspond to the orbital crossings discussed above (see *a*–*c* in Figures 1 and 5). The path of least energy (Figure 5, thick line) indicates that in the first stage there is substantial shortening of the O–O distance with only minor changes in the Mn–O lengths; this is consistent with the formation of a peroxo-bridged $Mn_2^{III,IV}$ species. Through a wide range of Mn–O distances the electronic structure of the molecule can be described as a superoxo-bridged $Mn_2^{III,III}$ species, then a loosely bound dioxygen-bridged $Mn_2^{II,III}$ complex is formed that finally falls apart with evolution of a dioxygen molecule.

Although we have used a rather crude model with high net charges at the two mononuclear units that result from dioxygen evolution, all the results indicate that the intramolecular dioxygen formation is electronically driven and not an artifact resulting from the Coulomb repulsion between the two Mn atoms in high oxidation states. Thus, we have performed calculations on a system with the $Mn_2^{IV,IV}$ oxidation state but with charges corresponding to the $Mn_2^{IV,V}$ complex (artificially achieved by increasing the nuclear charge of each Mn atom by 0.5). These calculations give essentially the same dioxo-bridged minimum; this indicates that no spontaneous dissociation occurs for the system with a net charge of +5 unless the number of valence electrons formally ascribed to the two Mn atoms becomes as low as 5 (i.e., considering the oxygen atoms as oxo ligands). We also note that, along the reaction pathway, the actual oxidation state of the Mn atoms may be, for example, $Mn^{III}/Mn^{III}$ (below point *c*, Figure 5) with a Mn–Mn distance of 2.7 Å. Yet systems with oxidation states as high as $Mn^{IV}/Mn^{IV}$ have similar Mn–Mn distances and are perfectly stable (see Tables 1–4).

Factors contributing to the higher stability of the $Mn_2^{II,III}$/dioxygen situation should include: 1) the formation of the O–O bond (–118 kcal mol$^{-1}$), 2) relaxation of the $Mn_2^{IV,IV}$ geometry to the $Mn_2^{IV,V}$ one (–35 kcal mol$^{-1}$, Figure 4), 3) relaxation of the dioxygen molecule from the singlet to the triplet state (–23 kcal · mol$^{-1}$) and 4) relaxation of the $Mn^{II}$ and $Mn^{III}$ mononuclear complexes to square planar geometry (about –50 kcal mol$^{-1}$ per Mn atom), although the latter may be prevented by the rigidity of the protein cage in PS II or by the bridging ligands present in model systems. Such stabilization is in part counterbalanced by the cleavage of the Mn–O bonds, two-electron terms associated with electron transfer from oxygen to Mn, and changes in coulombic repulsions within the $M_2O_2$ core.

## Conclusion

The results of the present theoretical study suggest that the oxygen-evolution step in PS II could proceed through intramolecular coupling of two bridging oxygen atoms, accompanied by oxygen to metal electron transfer. An important finding is that the oxidation of an oxo-bridged $Mn_2^{IV,IV}$ dinuclear complex removes an electron from the oxygen atoms, whereas the $Mn^V$ oxidation state cannot be attained within the $Mn_2O_2$ core because of its high relative energy. Thus, according to our calculations, the existence of a $Mn^V$ center in the $S_4$ state previous to nucleophilic attack of an $OH^-$ on a terminal oxo group is unlikely as long as the Mn atom forms an $Mn_2O_2$ rhombus. This oxidation triggers a cascade of oxygen-to-manganese one-electron transfer steps, coupled with cleavage of the Mn–O and formation of O–O bonds. A gradual conversion of delocalized to localized molecular orbitals is the reason underlying an energetically favorable process with no substantial energy barrier. Likely differences between our theoretical model and the $Mn_4$ cluster in the OEC are that, in the latter, complete dissociation into mononuclear $Mn^{II}$ and $Mn^{III}$ complexes may be prevented by the protein cage, and that the water molecules in the environment could easily bond to the coordinatively unsaturated Mn centers formed, thus regenerating the initial redox-active $Mn_2^{II,III}$ dinuclear unit in $S_0$. Since a catalytic cycle compatible with our results requires water uptake in the $S_4$ to $S_0$ transformation, one could expect that, in the presence of other good coordinating agents and at low water concentrations, the $S_0$ complex could be poisoned and the photocatalytic cycle interrupted.

We note that $M_2X_2$ cores similar to those studied in this paper are found in a variety of metalloenzymes playing

  0947-6539/02/0811-2514 $ 20.00+.50/0 *Chem. Eur. J.* **2002**, *8*, No. 11

diverse roles that include electron transfer (some ferredoxins and the $Cu_A$ center in blue copper proteins such as cytochrome C oxidase), oxygen binding (hemocyanins), peroxide dismutation (manganese catalase), organic-substrate oxygenation or oxidation (e.g., tyrosinase), and hydrogen oxidation (NiFe hydrogenases). The $M_2X_2$ cores of the active centers in these systems have different metal atoms (M = Mn, Fe, Ni, Cu) with varying oxidation states and coordination numbers, and oxygen or sulfur bridging atoms.[44] Most remarkable is the fact that similar rings are used by nature to bind (hemocyanin) or split (oxygenase) the dioxygen molecule and to effect the opposite reaction, that is, generate dioxygen from two water molecules (PS II). A deeper understanding of the similarities and differences in the electronic structure of such metalloenzymes is therefore a must if we wish to exert some control over the chemistry of such important biological processes or to design artificial systems that efficiently mimic them.

## Acknowledgements

Financial support to this work was provided by the Dirección General de Enseñanza Superior (DGES) through grant PB98-1166-C02-01 and by the Comissionat per a Universitats i Recerca (Generalitat de Catalunya) through grant SGR99-0046. The computing resources at the Centre de Supercomputació de Catalunya (CESCA) and Centre de Parallelisme de Barcelona (CEPBA) were made available in part through grants from the Comissió Interdepartamental per a la Recerca i la Innovació Tecnològica (CIRIT) and from the Universitat de Barcelona. The authors are grateful to W. B. Tolman, A. Aukaloo, and M. Corbella for critical reading of the manuscript and insightful suggestions, and to A. Lledós and C. Cramer for raising sensible questions on computational and theoretical aspects.

[1] J. Wikaira, S. M. Gorun in *Bioinorganic Catalysis*, 2nd ed. (Eds.: J. Reedijk, E. Bouwman), Marcel Dekker, New York, **1999**, p. 355.
[2] J. H. Robblee, R. M. Cinco, V. K. Yachandra, *Biochim. Biophys. Acta* **2001**, *1503*, 7.
[3] J. S. Vrettos, J. Limburg, G. W. Brudvig, *Biochim. Biophys. Acta* **2001**, *1503*, 229.
[4] G. M. Ananyev, L. Zaltsman, C. Vasko, G. C. Dismukes, *Biochim. Biophys. Acta* **2001**, *1503*, 52.
[5] A. Zouni, H.-T. Witt, J. Kern, P. Fromme, N. Krauss, W. Saenger, P. Orth, *Nature* **2001**, *409*, 739.
[6] B. Kok, B. Forbush, M. McGloin, *Photochem. Photobiol.* **1970**, *11*, 457.
[7] V. K. Yachandra, K. Sauer, M. P. Klein, *Chem. Rev.* **1996**, *96*, 2927.
[8] J. Limburg, V. A. Szalai, G. W. Brudvig, *J. Chem. Soc. Dalton Trans.* **1999**, 1353.
[9] T. J. Collins, S. W. Gordon-Wylie, *J. Am. Chem. Soc.* **1989**, *111*, 4511.
[10] T. J. Collins, R. D. Powell, C. Slebodnick, E. S. Uffelman, *J. Am. Chem. Soc.* **1990**, *112*, 899.
[11] C. G. Miller, S. W. Gordon-Wylie, C. P. Horwitz, S. A. Strazisar, D. K. Peraino, G. R. Clark, S. T. Weintraub, T. J. Collins, *J. Am. Chem. Soc.* **1998**, *120*, 11540.
[12] J. B. Vincent, G. Christou, *Inorg. Chim. Acta* **1987**, *136*, L41.
[13] W. Ruettinger, M. Yagi, K. Wolf, S. Bernasek, G. C. Dismukes, *J. Am. Chem. Soc.* **2000**, *122*, 10353.
[14] M. Yagi, K. V. Wolf, P. J. Baesjou, S. L. Bernasek, G. C. Dismukes, *Angew. Chem.* **2001**, *113*, 3009; *Angew. Chem. Int. Ed.* **2001**, *40*, 2925.
[15] J. Limburg, J. S. Vrettos, L. M. Liable-Sands, A. L. Rheingold, R. H. Crabtree, G. W. Brudvig, *Science* **1999**, *283*, 1524.
[16] J. Limburg, J. S. Vrettos, H. Chen, J. C. de Paula, R. H. Crabtree, G. W. Brudvig, *J. Am. Chem. Soc.* **2001**, *123*, 423.
[17] M. Yagi, M. Kaneko, *Chem. Rev.* **2001**, *101*, 21.
[18] J. E. McGrady, R. Stranger, *Inorg. Chem.* **1999**, *38*, 550.
[19] D. M. Proserpio, R. Hoffmann, G. C. Dismukes, *J. Am. Chem. Soc.* **1992**, *114*, 4374.
[20] P. E. M. Siegbahn, *Inorg. Chem.* **2000**, *39*, 2923.
[21] X. G. Zhao, W. H. Richardson, J.-L. Chen, J. Li, L. Noodleman, H.-L. Tsai, D. N. Hendrickson, *Inorg. Chem.* **1997**, *36*, 1198.
[22] S. Alvarez, P. Alemany, G. Aullón, A. A. Palacios, J. J. Novoa in *The Synergy Between Dynamics and Reactivity at Clusters and Surfaces* (Ed.: L. J. Farrugia), Kluwer, Dordrecht, **1995**, p. 241.
[23] X.-Y. Liu, A. A. Palacios, J. J. Novoa, S. Alvarez, *Inorg. Chem.* **1998**, *37*, 1202.
[24] A. A. Palacios, G. Aullón, P. Alemany, S. Alvarez, *Inorg. Chem.* **2000**, *39*, 3166.
[25] B. M. T. Lam, J. A. Halfen, V. G. Young, Jr., J. R. Hagadorn, P. L. Holland, A. Lledós, L. Cucurull-Sànchez, J. J. Novoa, S. Alvarez, W. B. Tolman, *Inorg. Chem.* **2000**, *39*, 4059.
[26] J. A. Halfen, S. Mahapatra, E. C. Wilkinson, S. Kaderli, V. G. Young, L. Que, A. D. Zuberbühler, W. B. Tolman, *Science* **1996**, *211*, 1397.
[27] J. Cahoy, P. J. Holland, W. B. Tolman, *Inorg. Chem.* **1999**, *38*, 2161.
[28] G. Aullón, P. Alemany, S. Alvarez, *J. Organomet. Chem.* **1994**, *478*, 75.
[29] P. E. M. Siegbahn, *Theor. Chem. Acc.* **2001**, *105*, 197.
[30] *Gaussian94*, Revision E.1, M. J. Frisch, G. W. Trucks, H. B. Schlegel, P. M. W. Gill, B. G. Johnson, M. A. Robb, J. R. Cheeseman, T. A. Keith, G. A. Petersson, J. A. Montgomery, K. Raghavachari, M. A. Al-Laham, V. G. Zakrzewski, J. V. Ortiz, J. B. Foresman, J. Cioslowski, B. B. Stefanov, A. Nanayakkara, M. Challacombe, C. Y. Peng, P. Y. Ayala, W. Chen, M. W. Wong, J. L. Andrés, E. S. Replogle, R. Gomperts, R. L. Martin, D. J. Fox, J. S. Binkley, D. J. Defrees, J. P. Baker, J. P. Stewart, M. Head-Gordon, C. Gonzalez, J. A. Pople, Gaussian, Inc., Pittsburgh PA, **1995**.
[31] A. D. Becke, *J. Chem. Phys.* **1993**, *98*, 5648.
[32] C. Lee, W. Yang, R. G. Parr, *Phys. Rev. B* **1988**, *37*, 785.
[33] S. Alvarez, A. A. Palacios, G. Aullón, *Coord. Chem. Rev.* **1999**, *185–186*, 431.
[34] E. Ruiz, P. Alemany, S. Alvarez, J. Cano, *J. Am. Chem. Soc.* **1997**, *119*, 1297.
[35] E. Ruiz, J. Cano, S. Alvarez, P. Alemany, *J. Comput. Chem.* **1998**, *20*, 1391.
[36] C. Adamo, V. Barone, *Chem. Phys. Lett.* **2000**, *330*, 152.
[37] M. Cosi, V. Barone, *J. Phys. Chem. A* **1998**, *102*, 1995.
[38] The energy of the antiferromagnetic state of a dinuclear complex is estimated in our calculations through the broken-symmetry approach.
[39] R. Manchanda, G. W. Brudvig, R. H. Crabtree, *Coord. Chem. Rev.* **1995**, *144*, 1.
[40] All the $J$ values in this paper correspond to the hamiltonian $H = -J\, S_1 \cdot S_2$.
[41] A. Caneschi, D. Gatteschi, R. Sessoli, *J. Chem. Soc. Dalton Trans.* **1997**, 3963.
[42] K. Wieghardt, *Angew. Chem.* **1994**, *106*, 765; *Angew. Chem. Int. Ed. Engl.* **1994**, *33*, 725.
[43] S. P. McGlynn, L. G. Vanquickenborne, M. Kinoshita, D. G. Carroll, *Introduction to Applied Quantum Chemistry*, Holt, Rinehart and Wilson, New York, **1972**.
[44] R. H. Holm, P. Kennepohl, E. I. Solomon, *Chem. Rev.* **1996**, *96*, 2239.

Received: October 22, 2001 [F3635]